



Publication Year	2021
Acceptance in OA	2022-01-05T10:08:01Z
Title	The diffuse ionized gas (DIG) in star-forming galaxies: the influence of aperture effects on local H II regions
Authors	MANNUCCI, FILIPPO, BELFIORE, FRANCESCO MICHEL CONCETTO, Curti, M., CRESCI, GIOVANNI, Maiolino, R., Marasco, A., Marconi, Alessandro, Mingozi, M., Tozzi, G., Amiri, A.
Publisher's version (DOI)	10.1093/mnras/stab2648
Handle	http://hdl.handle.net/20.500.12386/31314
Journal	MONTHLY NOTICES OF THE ROYAL ASTRONOMICAL SOCIETY
Volume	508

The diffuse ionized gas (DIG) in star-forming galaxies: the influence of aperture effects on local H II regions

F. Mannucci ¹★, F. Belfiore ¹, M. Curti,^{1,2,3} G. Cresci,¹ R. Maiolino,² A. Marasco ¹, A. Marconi,^{1,4} M. Mingozi,⁵ G. Tozzi^{1,4} and A. Amiri^{1,4}

¹INAF - Osservatorio Astrofisico di Arcetri, Largo E. Fermi 5, I-50125 Firenze, Italy

²Cavendish Laboratory, University of Cambridge, Madingley Rise, Cambridge, CB3 0HA, UK

³Kavli Institute for Cosmology, University of Cambridge, Madingley Rise, Cambridge, CB3 0HA, UK

⁴Dipartimento di Fisica e Astronomia, Università di Firenze, via G. Sansone 1, Sesto F.no, I-50019 Firenze, Italy

⁵Space Telescope Science Institute, 3700 San Martin Drive, Baltimore, MD 21218, USA

Accepted 2021 September 6. Received 2021 August 31; in original form 2021 June 14

ABSTRACT

The diffuse ionized gas (DIG) contributes to the nebular emission of galaxies, resulting in emission line flux ratios that can be significantly different from those produced by H II regions. Comparing the emission of [SII] λ 6717,31 between pointed observations of H II regions in nearby galaxies and integrated spectra of more distant galaxies, it has been recently claimed that the DIG can also deeply affect the emission of bright, star-forming galaxies, and that a large correction must be applied to observed line ratios to recover the genuine contribution from H II regions. Here, we show instead that the effect of DIG on the integrated spectra of star-forming galaxies is lower than assumed in previous work. Here we show that, in contrast, aperture effects on the spectroscopy of nearby H II regions are largely responsible for the observed difference: When spectra of local H II regions are extracted using large enough apertures while still avoiding the DIG, the observed line ratios are the same as in more distant galaxies. This result is highly relevant for the use of strong-line methods to measure metallicity.

Key words: ISM: abundances – H II regions – galaxies: abundances – galaxies: ISM.

1 INTRODUCTION

Emission lines are a fundamental probe of the physical properties of the interstellar medium (ISM) and reveal a large number of characteristics of the emitting galaxies, such as star formation rates (SFR), gas-phase metallicity and abundance ratios, dust extinction, dynamical mass, presence of outflows, and presence of an active galactic nucleus (AGN). In many cases, optical emission lines are dominated by ionization by young, massive stars, but different ionization sources are also present. Specifically, shocks and hot, evolved stars can contribute to the total emission (see e.g. Peimbert, Peimbert & Delgado-Inglada 2017; Kewley, Nicholls & Sutherland 2019; Maiolino & Mannucci 2019).

Most of our knowledge of the distant universe comes from spectra of spatially unresolved or poorly resolved (>1 kpc) galaxies. Even if spectra are often modelled by the emission of single, homogeneous H II region, reality is clearly not that simple. Galaxies contain a complex, multiphase ISM characterised by different values of density, temperature, ionization, and metallicity.

The warm ($T_e \sim 10^4$ K), ionized component of the ISM can be subdivided into H II regions, where hydrogen is fully ionized by hot, young stars, and the diffuse ionized gas (DIG), a more diffuse medium found outside H II regions, and particularly evident above and below the galactic plane.

With respect to H II regions, the DIG is characterised by lower densities, lower ionization parameters, a harder ionizing spectrum, a potential presence of shocks, lower equivalent widths (EW) of line emission, and a lower surface brightness (SB) (Reynolds 1984; Minter & Balser 1997; Hidalgo-Gómez 2005; Haffner et al. 2009; Belfiore et al. 2016; Kumari et al. 2019; Vale Asari et al. 2019; Della Bruna et al. 2020; Tomicic et al. 2021). As a consequence, the DIG shows line ratios that could differ substantially from those observed in H II regions, with much stronger emission of the low ionization lines as [OII] λ 3726,29 and, in particular, [SII] λ 6717,31 (e.g., Zhang et al. 2017).

The DIG consists of several, physically distinct components that should not be confused even if they are given the same name. (1) Part of the DIG is ionized by photons from young, hot stars leaking out of the H II regions, and ionizing gas at larger distances, at lower densities, producing lower ionization parameters. (e.g. Ferguson et al. 1996; Voges & Walterbos 2006). This gas sees an ionizing spectrum similar to that of the H II region, hardened by partial absorption (e.g. Giammanco et al. 2004; Zhang et al. 2017). Its position in the Baldwin-Phillips-Terlevich (BPT) diagram ([O III] λ 5007/H β versus [N II] λ 6584/H α) is generally expected to be the same as H II regions, with similar emission line ratios (Zhang et al. 2017, Belfiore et al., in prep). Clearly, there is a continuity between the properties of H II regions and of the surrounding DIG, and there is no clear boundary between the two. Being produced by the hot, young stars, the amount of this ‘leaking-DIG’ is expected to be proportional to the SFR, as the emission from the H II regions. As such, it is dominant in

* E-mail: filippo.mannucci@inaf.it

star-forming galaxies. (2) Part of the DIG is ionized by old, post-AGB stars, sometimes named HOLMES (hot low-mass evolved stars). This ‘HOLMES-DIG’ component is dominant in quenched galaxies with no or low levels of star formation (e.g. Byler et al. 2019). Emission line flux ratios can be very different from those from H II regions and their position on the BPT diagram is in the low-ionization emission-line region (LIER) part (Kumari et al. 2019). Its relative contribution to line emission is expected to change greatly from galaxy to galaxy, depending on the specific SFR (sSFR), and with cosmic time. (3) Part of the DIG is due to ionization by shocks or by the hot-cold gas interface (e.g. Rand 1998; Collins & Rand 2001; Haffner et al. 2009; Zhang et al. 2017; Tomićić et al. 2021). This ‘shocked-DIG’ also produces line ratios in the LIER part of the BPT diagram, and can also be revealed by larger line widths (Tüllmann & Dettmar 2000; Hidalgo-Gómez 2005). Its contribution is related to the star-formation activity (e.g. Rossa & Dettmar 2003), and can be particularly evident at high galactic latitudes and at large distances from the disc.

HOLMES-DIG and shocked-DIG are preferentially selected when either BPT diagrams and/or cuts in $EW(H\alpha)$ are used (e.g. Lacerda et al. 2018; Kumari et al. 2019; Law et al. 2021, see Fig. 2 and section 2.1.)

In contrast, when H II regions are (often subjectively) isolated from the surrounding medium based on morphology or SB of the emission lines, the remaining emission is usually dominated by leaking-DIG. Throughout this paper, we do not consider the ISM ionized by the hard radiation typical of AGNs.

The influence of DIG on the integrated properties of galaxies is subject of active debate. The DIG gives an important contribution to the emission of the Milky Way (e.g. Zurita, Rozas & Beckman 2000) and of the local galaxies (e.g. Oey et al. 2007; Della Bruna et al. 2020; Tomićić et al. 2021): depending on the definition, this contribution can be even larger than 90 per cent. In more distant galaxies, however, the contribution of the DIG to the total line emission cannot be measured directly. In most cases, only integrated spectra, or spectroscopy with poor spatial resolution, are available, and it is not possible to spatially separate H II regions and the DIG. As the total spectrum is a flux-weighted sum of all the emission, the much larger SB of H II regions can easily dominate the emission as soon as the SFR is significant, nevertheless the underlying contribution of DIG can alter the observed emission line flux ratios.

A large influence of the DIG on the spectra of star-forming galaxies would have a significant impact on many results on the determination of their physical properties. In particular, the methods to measure ISM metallicity from the strong-line ratios (see e.g. Maiolino & Mannucci 2019) are calibrated on H II regions or on star-forming galaxies, and cannot be safely applied on galaxies with different levels of contribution from the DIG due to different levels of sSFR. Also, contamination from DIGs would significantly affect our picture of the evolution of the mass-metallicity relation (MZR, e.g. Tremonti et al. 2004) and of the Fundamental metallicity relation (FMR, e.g. Mannucci et al. 2010).

A promising method to quantify the contribution of the DIG is to compare the spectra of local H II regions with the integrated spectra of galaxies. The DIG contribution to the former set of spectra is expected to be negligible, while the intrinsic properties of nearby and distant H II regions are expected to be similar. With these two assumptions the differences in spectra can be attributed to the contribution of DIG to the spectra using apertures much larger than the H II regions.

This method was recently employed, for example, by Sanders et al. (2017) and Sanders et al. (2019), who compared the spectra in nearby, H II regions observed using pointed long-slit spectra, with integrated spectra, like the SDSS (Abazajian et al. 2009), or with

low resolution, kpc-scale spectra like CALIFA (Sánchez et al. 2012) and MaNGA (Bundy et al. 2015). They revealed large differences in some line ratios, in particular in those including the low ionization $[SII]\lambda 6717,31$ doublet. Here, we will show that this difference is actually dominated by aperture effect in the local sample of H II regions.

1.1 Radial dependence of line ratios and aperture effects

H II regions are expected to be stratified. Specifically, higher ionization species like O^{++} and S^{++} dominate the inner regions, closer to the ionizing source, while lower ionization species are more abundant in the outer part. The ionization structure of a spherically symmetric H II region around an ionization source can be theoretically computed with dedicated software, such as CLOUDY (Ferland et al. 2013) or MAPPINGS (Dopita et al. 2014). H II region models have been presented in many works (see for example, Levesque, Levesque & Larson 2010; Pellegrini et al. 2012; Xiao, Stanway & Eldridge 2018; and Kewley et al. 2019). The high-ionization lines like $[OIII]\lambda 5007$ and $[SIII]\lambda 9069,9531$ are emitted by the inner part of the regions, surrounded by the intermediate- ($[NII]\lambda 6854$) and low-ionization lines ($[OII]\lambda 3727$ and $[SII]\lambda 6717,31$). For example, Xiao et al. (2018) find a ~ 0.6 dex increase in the $[SII]\lambda 6717,31/H\alpha$ ratio between the central and outer part of their modelled H II regions. This effect is exemplified in Fig. 1, which shows the results of CLOUDY model for a H II region ionized by a 2 Myr-old simple stellar population, with density of 10^2 cm^{-3} , metallicity $[Fe/H] = -0.2$, and ionization parameter $\log(U) = -3.5$. The input spectrum is generated using the flexible stellar population synthesis code FSPS v3.1 of (Conroy, Gunn & White 2009) and MIST isochrones (Choi et al. 2016; Dotter 2016). More details are presented in Belfiore et al., in prep. The models show that most of the low ionization lines from O^+ and, in particular, S^+ (left hand) are emitted by the outer shell of the H II region. As a consequence, the line ratios (right hand) have a strong radial dependence: for example $\log([SII]\lambda 6717,31/H\alpha)$ changes by more than one order of magnitude, from -0.4 near the inner edge of the ionized gas to $+0.7$ near the outer edge. As a consequence, spectra covering only the inner part of an H II regions would show line ratios which are not representative of the entire region.

The spectra of nearby H II regions are, in most cases, obtained using long slits with typical apertures of 1–2 arcsec, giving physical spatial scales of 10–50 pc at distances of a few Mpc (Pilyugin, Grebel & Mattsson 2012). The recent catalog of H II spectra of the CHAOS project (Berg et al. 2015; Croxall et al. 2015, 2016; Berg et al. 2020) is often used because of its high S/N ratio, large spectral coverage, homogeneity, and number of targets. This catalog is based of high-quality LBT observations of about 200 H II regions in three galaxies (NGC 628, M51, and M101), between 7.2 and 9.8 Mpc, for which the 1 arcsec slit width samples ~ 35 –45 pc. Recently, the CHAOS team has published data for one additional galaxy, NGC 2403, much closer than the others and, as a consequence, sampling even smaller physical sizes (Rogers et al. 2021).

1.2 H II region size

H II region radii scale with luminosity following a well-defined relation (e.g. Kennicutt 1984; Youngblood & Hunter 1999; Oey et al. 2003; Ferreira & Pastoriza 2004; Pellegrini et al. 2012; Wisnioski et al. 2012; Beaton et al. 2014; Cosens et al. 2018). This relation is shown in Fig. 3, together with the linear fit by Cosens et al. (2018). At the typical $H\alpha$ luminosities targeted by the CHAOS project, shown

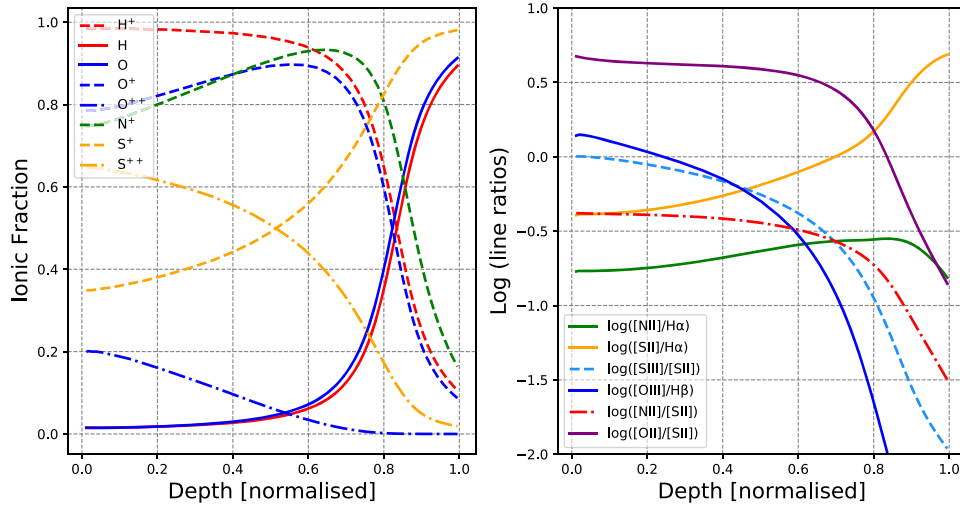


Figure 1. Expected ionization structure (left) and emission line flux ratios (right) of a spherically-symmetric H II region as computed by CLOUDY for a 2 Myr-old simple stellar population, density of 10^2 cm^{-3} , metallicity $[\text{Fe}/\text{H}] = -0.2$, and ionization parameter $\log(U) = -3.5$. The quantities are shown as a function of the fractional depth, i.e. the distance from the illuminated face of the emitting cloud.

Table 1. Properties of the galaxy sample.

Galaxy	Distance (Mpc)	Scale (pc/arcsec)	Central $12+\log(\text{O}/\text{H})$
NGC 628	9.8 ¹	47	8.83 ²
NGC 7793	3.6 ¹	17	8.50 ³
NGC 1705	5.2 ⁴	25	7.96 ⁵

Note. ¹Anand et al. (2021); ²Berg et al. (2015); ³Pilyugin, Grebel & Kniazev (2014); ⁴Sabbi et al. (2018); ⁵Annibali et al. (2015).

by the green band containing 90 per cent of sample, the H II region diameters are between 80 and 800 pc, while the 1 arcsec slit samples between 35 and 55 pc. Using apertures smaller than these size scales, may therefore, result in biased line ratios, because the spectroscopic aperture would collect only a low fraction of $[\text{SII}]\lambda 6717,31/\text{H}\alpha$. Evidences of varying line ratios along slits centered on H II regions and long enough to cover the surrounding regions have been found in nearby galaxies for distance scales of ~ 100 pc (Hoopes & Walterbos 2003; Voges & Walterbos 2006), even if long-slit spectra cannot recover the full emission of a spatially resolved H II region.

In this work, we want to use integral-field-unit (IFU) spectra to test if this aperture effect is present in the CHAOS data, and what its consequences are in estimating the contribution of the DIG in integrated spectra of galaxies.

2 INTEGRATED, DIG-FREE SPECTRA OF NEARBY H II REGIONS

To study the effect of aperture choice on line ratios, we have selected three local galaxies, with distance below ~ 10 Mpc, across a large range of metallicity, and for which MUSE/VLT IFU spectra are available, see Table 1. MUSE spectra cover the optical wavelength range from 0.46 to $0.93 \mu\text{m}$ and allow us to observe most of the bright emission lines that characterise star-forming galaxies in the local universe. The large field-of-view (FoV) and high sampling (0.2 arcsec/spaxel) of the instrument, together with the excellent seeing at Paranal (typically 0.6–0.8 arcsec FWHM) allow us to sample scales of 20–30 pc, below the typical dimensions of average-luminosity H II regions (see e.g. Wisnioski et al. 2012 and Beaton et al. 2014).

Line fluxes were obtained for each spaxel of the datacube by a multi-Gaussian fit to each emission line, as described in Marasco et al. (2020). We have used these IFU spectra to study the effect of different apertures on the resulting spectra, avoiding any contribution from the DIG.

2.1 DIG definition

Commonly, DIG is defined using the $\text{H}\alpha$ line, selecting regions with either low $\text{SB}(\text{H}\alpha)$, or low $\text{EW}(\text{H}\alpha)$. Conversely, H II regions are identified with regions of high $\text{SB}(\text{H}\alpha)$ or high $\text{EW}(\text{H}\alpha)$, once AGN-dominated regions are removed. The two definitions are physically different but, at least in local galaxies, lead to similar results.

The definition based on $\text{SB}(\text{H}\alpha)$ is motivated both by the observed change in line ratios with SB (Oey et al. 2007), and the physical expectations from leaking photons from H II regions. High-resolution studies of local galaxies divide H II regions from DIG regions using SB down to $10^{37.6} \text{ erg/s/kpc}^2$ (Ferguson et al. 1996; Hoopes, Walterbos & Greenwalt 1996; Della Bruna et al. 2020). Here, we follow Zhang et al. (2017) and Kumari et al. (2019) and use a significantly higher threshold, defining a region as H II-dominated if it has $\text{SB}(\text{H}\alpha) > 10^{39} \text{ erg/s/kpc}^2$, value at which the line ratios start to change significantly. Our results do not depend critically on the use SB threshold, and changing its value by ± 0.5 dex does not change the conclusions. The DIG contribution to these regions, is therefore, expected to be negligible.

Using spatially resolved data from CALIFA, Lacerda et al. (2018) proposed a scheme where the emitting regions can be divided into three classes based on $\text{EW}(\text{H}\alpha)$. The DIG dominates regions with $\text{EW}(\text{H}\alpha) < 3 \text{ \AA}$, at $\text{EW}(\text{H}\alpha) > 14 \text{ \AA}$, the ionization is purely due to H II regions, while in between there are various levels of mixing. They showed that $\text{EW}(\text{H}\alpha)$ correlates tightly with the position on the BPT diagrams, with regions with $\text{EW}(\text{H}\alpha) > 14 \text{ \AA}$ having line ratios typical of H II regions. Also, only $\text{EW}(\text{H}\alpha) < 3 \text{ \AA}$ are observed in early type galaxies, while in galaxies later than Sc are dominated by regions with $\text{EW}(\text{H}\alpha) > 14 \text{ \AA}$. Finally, extraplanar emission, far from star-forming regions, is dominated by low $\text{EW}(\text{H}\alpha)$ regions, while discs are dominated by high $\text{EW}(\text{H}\alpha)$ regions.

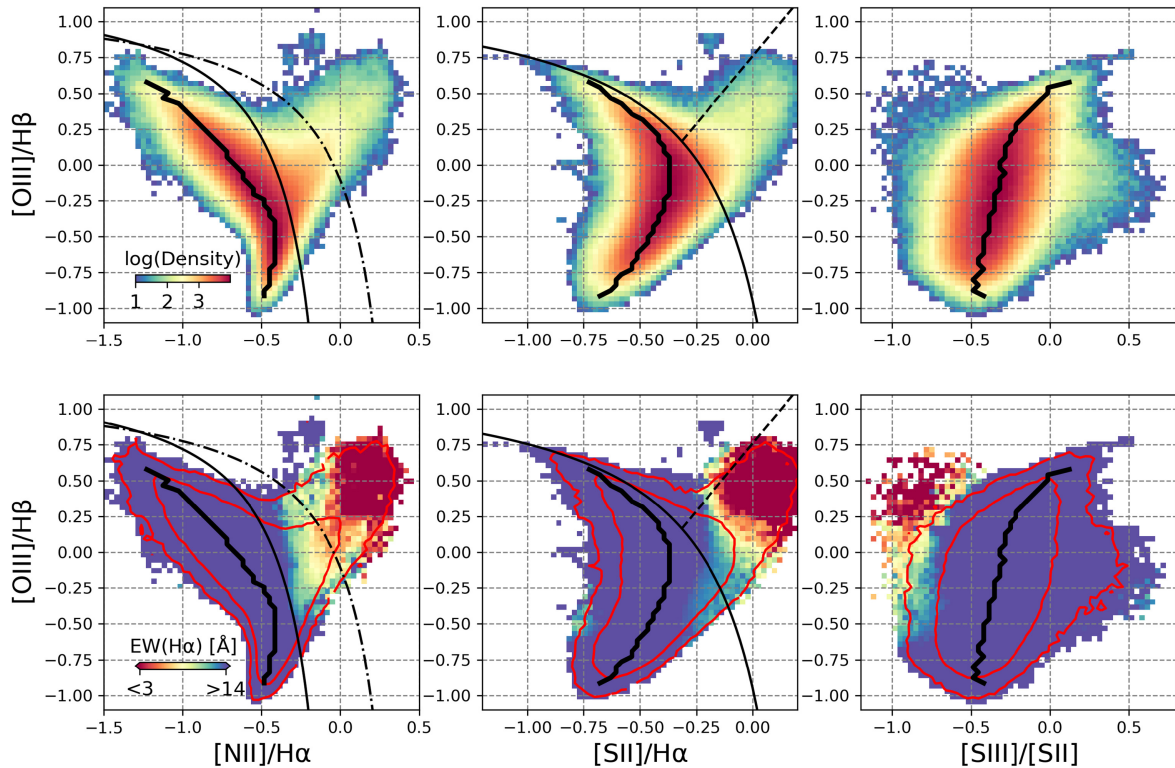


Figure 2. BPT diagrams for the single spaxels in MaNGA, plotting $[\text{O III}]\lambda 5007/\text{H}\beta$ versus either $[\text{N II}]\lambda 6584/\text{H}\alpha$ ([N II]-BPT, left), $[\text{S II}]\lambda 6717,31/\text{H}\alpha$ ([S II]-BPT, center), or $[\text{S III}]\lambda 9069,9531/[\text{S II}]\lambda 6717,31$ ([S III]-BPT, right). The upper panels show the density of points, while the lower panels show the median $\text{EW}(\text{H}\alpha)$ in each bin from 3\AA (red points) to 14\AA (blue points). The separation lines are from Kauffmann et al. (2003) and Kewley et al. (2001). The thick, black line shows the median line ratios for the star-forming galaxies in bins of $[\text{O III}]\lambda 5007/\text{H}\beta$. Spaxels are selected from all MaNGA galaxies included in DR15 Aguado et al. (2019) and with $\text{S/N} > 5$ on the required emission lines in each diagram. Fluxes are obtained from the publicly-available maps generated by the MaNGA data analysis pipeline (Belfiore et al. 2019; Westfall et al. 2019). AGN hosts, defined as MaNGA galaxies where the spectrum extracted from a 3 arcsec aperture around the galaxy centre falls in the AGN corner of the [S II]-BPT diagram according to the demarcation lines of Kewley et al. (2006), are removed.

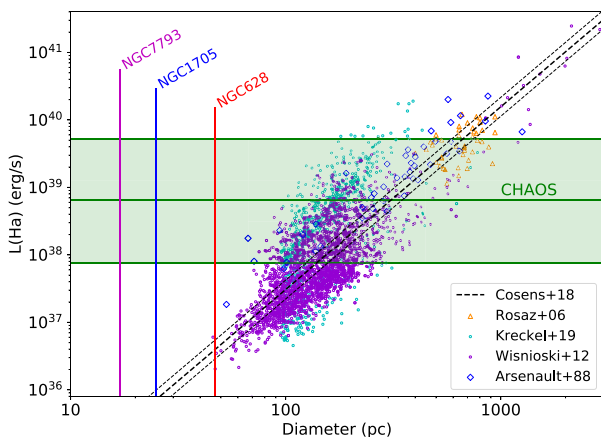


Figure 3. Size-luminosity relation for H II regions in nearby galaxies. The black, dashed lines show the average correlation and its scatter from the large compilation of data in Cosens et al. (2018). Dots are data for single regions from Arsenault & Roy (1988), Rosaz et al. (2006), Wisnioski et al. (2012), and Kreckel et al. (2019). The green band shows the characteristic luminosity of the CHAOS H II regions and contains 90 per cent of this sample. The vertical lines correspond to 1 arcsec at the distance of the three galaxies of our sample. It is apparent that only the central, high ionization parts of the CHAOS H II regions are sampled by the 1 arcsec slit.

The strong relation between $\text{EW}(\text{H}\alpha)$ and position on the BPT can also be seen in the MaNGA data, as shown in Fig. 2 (Belfiore et al. 2019; Westfall et al. 2019; Mingozi et al. 2020): When the 4686 AGN-hosting galaxies (~ 9 per cent of the total sample) are removed using the central spectrum, the remaining spaxels with high $\text{EW}(\text{H}\alpha)$ also have line ratios typical of star-forming galaxies, while gas ionized by shock and post-AGB stars shows low values of $\text{EW}(\text{H}\alpha)$.

We have applied these two DIG definitions based on $\text{EW}(\text{H}\alpha)$ and $\text{SB}(\text{H}\alpha)$ to our sample of galaxies. In Fig. 4, we show the maps of stellar continuum, $\text{H}\alpha$ luminosity, $\text{EW}(\text{H}\alpha)$ and $\text{SB}(\text{H}\alpha)$, for the three fields. In all galaxies compact, bright regions are present together with a more diffused, low $\text{SB}(\text{H}\alpha)$, and low $\text{EW}(\text{H}\alpha)$ emission. The colour-coding in the $\text{EW}(\text{H}\alpha)$ and $\text{SB}(\text{H}\alpha)$ maps is such that, in both cases, regions totally dominated by H II emission ($\text{EW}(\text{H}\alpha) > 14\text{\AA}$ or $\text{SB}(\text{H}\alpha) > 10^{39}\text{ erg/s/kpc}^2$) are shown in blue, and DIG-dominated regions ($\text{EW}(\text{H}\alpha) < 3\text{\AA}$ or $\text{SB}(\text{H}\alpha) < 10^{38}\text{ erg/s/kpc}^2$) are shown in red. Intermediate colours map regions with both contributions. The two classification schemes are very similar, with a good match even on the scale of individual spaxels. In this work, we use the definition of DIG based on $\text{EW}(\text{H}\alpha)$, but the results do not depend much on this choice.

2.2 Spectra of H II regions of different apertures

In the three fields, we selected a representative sample of the 11 H II regions showing the brightest $\text{H}\alpha$ emission, see Table 2.

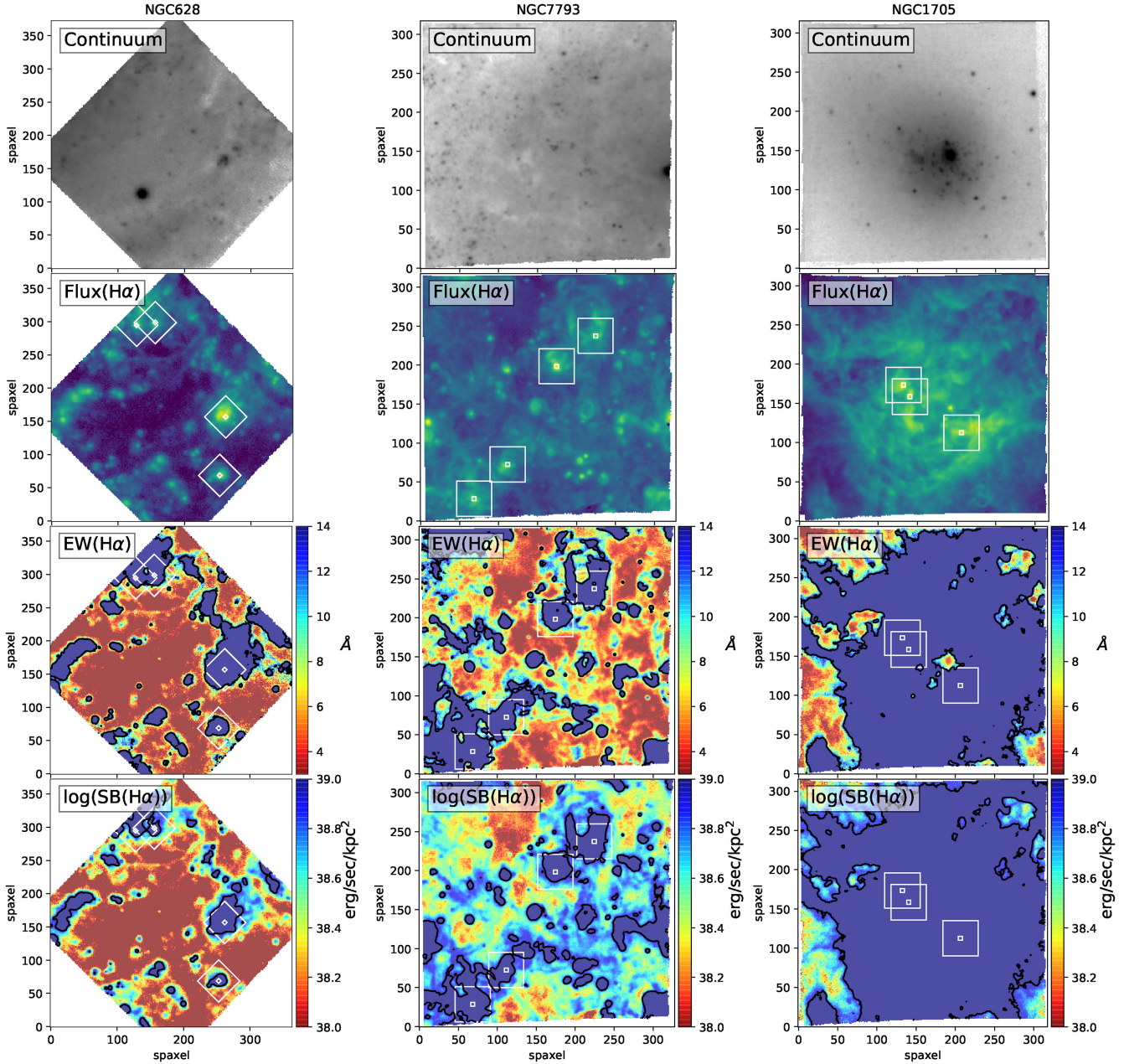


Figure 4. Maps of the three fields belonging to, from left to right, NGC 628, NGC 7793, and NGC 1705, sorted according to decreasing metallicity. For each galaxy we show, from top to bottom, maps of the stellar continuum in log scale, the continuum-subtracted H α flux in log scale, EW(H α), and SB(H α) in log scale. The full $1' \times 1'$ FoV of MUSE is shown. The white boxes have dimensions of 1×1 arcsec (corresponding to 17–47 pc, see Table 1) and 9×9 arcsec and show the H II regions used to extract the spectra used for Fig. 5. The blue regions in the lower two rows have either EW(H α) > 14 Å or SB(H α) > 10^{39} erg/s/kpc² and, as a consequence, can be considered as dominated by genuine H II emission and free from important contributions from the DIG. The regions dominated by the DIG are shown in red, while the intermediate colours show composite regions. It is evident that the fractional area of the galaxy dominated by H II emission increases with decreasing metallicity.

These regions are always characterised by high EW(H α) and high SB(H α), showing that they are dominated by ionization by hot, young stars. These are the regions usually observed in pointed H II observations like CHAOS. Their luminosity, $L(\text{H}\alpha) \sim 10^{38}$ erg/s, places them among the typical H II regions and significantly below the giant H II regions [$L(\text{H}\alpha) \sim 10^{40}$ erg/s] Ferreiro & Pastoriza 2004; Helmboldt et al. 2005; Bradley et al. 2006].

Spectra with apertures of 1×1 arcsec are extracted at the position of each H II region, to reproduce what is usually observed by long-

slit observations. This aperture corresponds to 15–45 pc, depending on the galaxy distance, similar to or smaller than what is sampled by CHAOS (typically 45 pc). As MUSE only covers the wavelength range between 0.46 and 0.93 μm , the total flux of the [SIII] doublet is obtained by using the theoretical flux ratio $[\text{SIII}]\lambda 9531/[\text{SIII}]\lambda 9069 = 2.47$ as used in PYNEB (Luridiana, Morisset & Shaw 2015; Mingozi et al. 2020). A second spectrum is extracted at the same position with apertures up to 9×9 arcsec (140–420 pc), large enough to sample most of the H II region emission. This aperture also mimics

Table 2. List of the H II regions used, including the coordinated, the luminosity of H α inside the 9×9 arcsec aperture, and the relevant line ratios inside the 1×1 arcsec and 9×9 arcsec apertures.

H II region	RA	DEC	L(H α) 10^{38} erg/s	log([N II] λ 6584/H α)		log([O III] λ 5007/H β)		log([S II] λ 6717/H α)		log([S III] λ 9069/[S II] λ 6717,31)	
				1 arcsec	9 arcsec	1 arcsec	9 arcsec	1 arcsec	9 arcsec	1 arcsec	9 arcsec
NGC 628 A	01:36:36.73	+15:46:33.8	6.34	-0.54	-0.55	-0.43	-0.70	-0.76	-0.65	+0.19	-0.10
NGC 628 B	01:36:38.53	+15:47:00.8	1.52	-0.53	-0.53	-0.91	-0.68	-0.80	-0.62	+0.06	-0.41
NGC 628 C	01:36:36.78	+15:46:15.6	0.965	-0.61	-0.54	-0.80	-0.78	-0.89	-0.66	+0.14	-0.23
NGC 628 D	01:36:38.15	+15:47:01.4	1.38	-0.56	-0.53	-0.90	-0.68	-0.80	-0.61	+0.08	-0.37
NGC 7793 A	23:57:52.01	-32:35:14.2	0.757	-0.92	-0.71	+0.27	+0.35	-0.94	-0.50	+0.55	-0.16
NGC 7793 B	23:57:53.04	-32:35:39.8	0.437	-0.90	-0.70	-0.26	-0.23	-0.92	-0.49	+0.38	-0.12
NGC 7793 C	23:57:52.70	-32:35:48.5	0.635	-0.81	-0.77	-0.67	-0.36	-0.67	-0.51	+0.01	-0.21
NGC 7793 D	23:57:51.23	-32:35:06.9	0.553	-0.71	-0.60	-0.14	-0.26	-0.68	-0.39	+0.05	-0.30
NGC 1705 A	04:54:14.65	-53:21:37.1	14.6	-1.43	-1.31	+0.68	+0.61	-0.99	-0.77	+0.31	-0.07
NGC 1705 B	04:54:14.83	-53:21:37.1	11.9	-1.52	-1.28	+0.59	+0.54	-1.04	-0.73	+0.31	-0.12
NGC 1705 C	04:54:13.18	-53:21:46.1	17.2	-1.58	-1.38	+0.67	+0.68	-1.04	-0.89	+0.25	+0.04

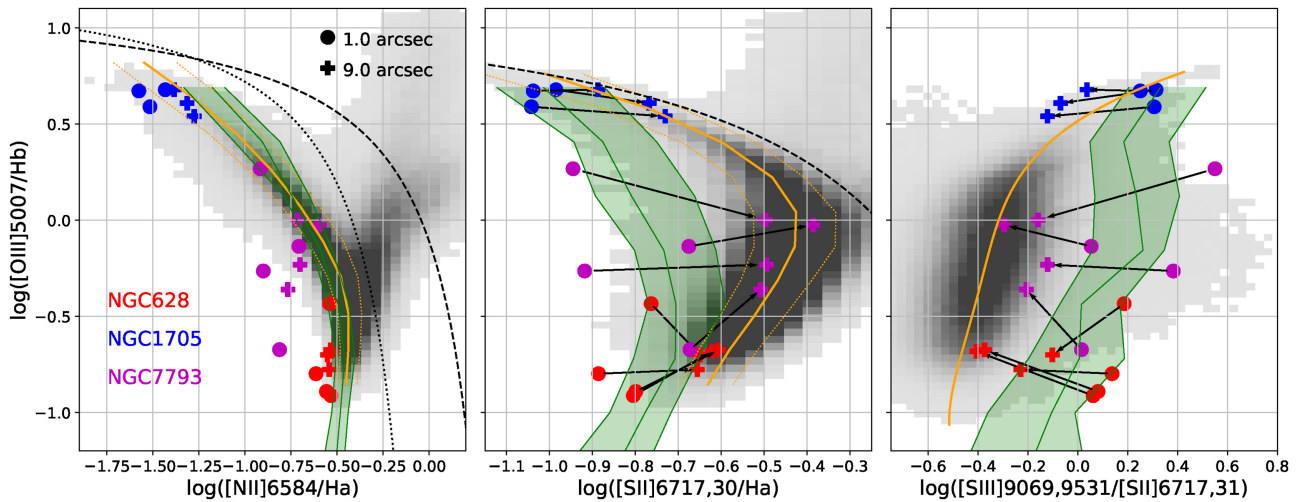


Figure 5. BPT diagrams plotting $[\text{O III}]\lambda 5007/\text{H}\beta$ versus $[\text{N II}]\lambda 6584/\text{H}\alpha$ (left), $[\text{S II}]\lambda 6717,31/\text{H}\alpha$ (center), and $[\text{S III}]\lambda 9069,9531/[\text{S II}]\lambda 6717,31$ (right). Circles show line ratios extracted from 1×1 arcsec apertures, crosses from 9×9 arcsec aperture. Arrows link the points relative to the same region. The grey-scale image in the left and central panels show the distribution of SDSS-DR7 galaxies, with the orange lines showing the medians of the distribution. The distribution from MaNGA galaxies (not shown) is perfectly coincident with that from SDSS. In the right hand, the grey-scale image and the orange line are from MaNGA spaxels. The dotted and dashed black lines separate galaxies dominated by star formation and by AGNs, and are from Kauffmann et al. (2003) and Kewley et al. (2001), respectively. The green band shows the position of the H II regions in the CHAOS project from Berg et al. (2015), Croxall et al. (2015), and Croxall et al. (2016), with the lines showing the 25th, 50th, and 75th percentiles.

the area covered by IFU surveys such as CALIFA or MaNGA. The fibers used for these surveys are physically smaller (2 and 3 arcsec, respectively), but the target galaxies are usually more distant. Inside these apertures, only H II spaxels, i.e. with $\text{EW}(\text{H}\alpha) > 14 \text{ \AA}$, were considered, all the spaxels below this threshold are masked out. This procedure produces an integrated spectrum of the H II regions avoiding contamination by the DIG. As a consequence, these two spectra refer to the same DIG-free H II region but with two different physical coverage, few tens of pc for the 1 arcsec aperture, and few hundreds of pc for 9 arcsec, sampling most of the H II regions (even if the H II regions in the galaxy with the lowest metallicity can be even more extended).

3 RESULTS

The results on several line ratios are presented in Fig. 5. Circles and crosses show the results using small and large apertures, respectively. The grey-scale images and orange lines show kpc-scale spectra from SDSS and MaNGA with $\text{S/N} > 5$ for each line, $\text{S/N} > 3$

for $[\text{S III}]\lambda 9069,9531$. The green-shaded area show the positions of single H II regions from the CHAOS project.

The aperture has hardly any effect of the $[\text{N II}]\lambda 6584/\text{H}\alpha$ and $[\text{O III}]\lambda 5007/\text{H}\beta$ line ratios, as shown in the left hand of the figure.

In contrast, line ratios involving $[\text{S II}]\lambda 6717,31$ are deeply affected. $[\text{S II}]\lambda 6717/\text{H}\alpha$ (middle panel) increases significantly when increasing the aperture. The line ratios obtained with the small apertures are consistent with those obtained by CHAOS, while when using large aperture the results are similar to what was obtained by SDSS and MaNGA. Same effect is seen for the $[\text{S III}]\lambda 9069,9531/[\text{S II}]\lambda 6717,31$ (lower panel): The ratio decreases significantly with aperture, becoming consistent with MaNGA at large apertures. Large-aperture line ratios are also consistent with those obtained by Kreckel et al. (2019) for a sample of nearby H II regions with luminosities ($L(\text{H}\alpha) \sim 10^{37} - 10^{39}$ erg/s) and spectroscopic apertures ($d = 40 - 200$ pc) similar to our sample. We stress that the large apertures are still inside the H II boundary as defined above and avoid any significant contribution from DIG.

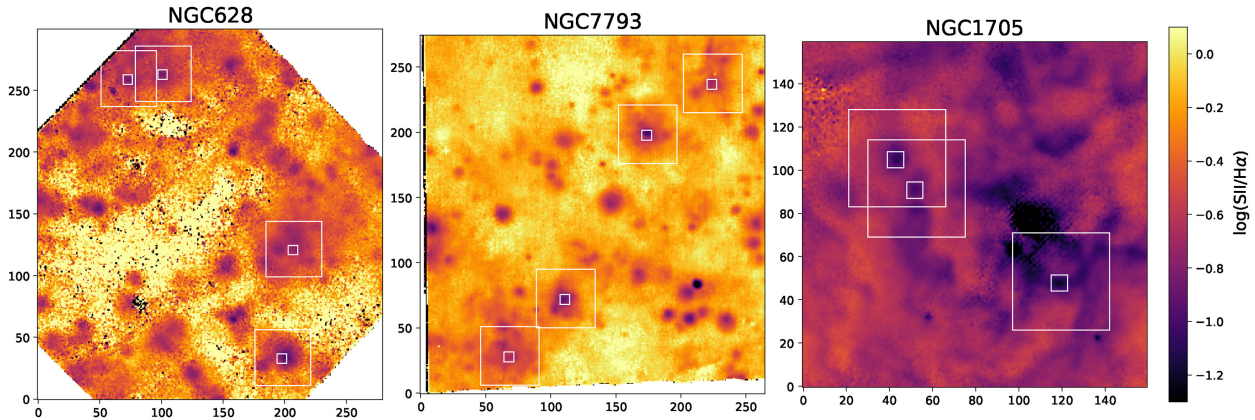


Figure 6. Flux ratio $[\text{SII}]\lambda 6717,31/\text{H}\alpha$ for the three fields. The H II regions considered are shown by white boxes of 1 and 9 arcsec of side. The ratio in the center of the boxes, corresponding to the peak of $\text{H}\alpha$ emission, is considerably lower than that of the surrounding regions.

This dependence of line ratios on apertures can also be directly seen in the map of the line ratio, as shown in Fig. 6. We can only present the $[\text{SII}]\lambda 6717,31/\text{H}\alpha$ line ratio because $[\text{SIII}]\lambda 9531$ is outside the MUSE wavelength range, and $[\text{SIII}]\lambda 9069$ is too faint to be detected in individual spaxels outside the core of the H II regions. The average value of this ratio is determined by the metallicity of the galaxy (e.g. Curti et al. 2020). Compared to the average value, this ratio has clear minima close to the center of the H II regions, where $\text{SB}(\text{H}\alpha)$ is maximum, with dimensions of a few arcsec, and shows a significant radial increase, even inside the region with large $\text{EW}(\text{H}\alpha)$. This shows that the H II regions are actually resolved in the galaxies at 3–10 Mpc of distances, and the ionizing structure in Fig. 1 can be observed.

These results show that the difference in low-ionization line fluxes between local H II regions and galaxies outside the Local Group is dominated by aperture effects in the local sample. The outputs of the photoionization models should be better compared with the total spectra of H II regions obtained with larger physical apertures. Overall, the unresolved or partially-resolved spectra from SDSS and MaNGA seem to be dominated by H II emission and do not show strong contribution from the DIG. For this reason, high-redshift galaxies with high specific SFRs and low levels of DIG contamination are expected to have spectra more similar to SDSS and MaNGA rather than to the spectra of the over-resolved H II regions. In fact, Sanders et al. (2019) showed that the MOSDEF galaxies at $z \sim 1.5$ have $[\text{SII}]\lambda 6717,31/\text{H}\alpha$ and $[\text{SIII}]\lambda 9069,9531/[\text{SII}]\lambda 6717,31$ line ratios totally consistent with the local SDSS and MaNGA spectra. Finally, applying large DIG corrections based on the local H II regions when using strong-line methods to compute metallicities may lead to biased results.

4 SUMMARY

H II regions in local galaxies show different properties from the total or kpc-scale spectra of star-forming galaxies when the flux ratios involving low-ionization emission lines are considered. This difference is often attributed to an increasing contribution of the DIG, absent in the local H II regions but deeply affecting galaxy spectra when regions of a few kpc are sampled. We have studied if aperture effects in spectra of H II regions in local galaxies can contribute to the differences.

We have selected a number of H II regions in local galaxies for which MUSE IFU spectra are available. To obtain spectra of

the whole H II regions, we have used different apertures while avoiding spaxels showing significant contribution from the DIG. The spectra from small and large apertures show remarkable differences, especially in the $[\text{SII}]\lambda 6717,31$ low ionization doublet. When using small, 1 arcsec apertures, the line ratios are similar to what was observed by long-slit surveys as CHAOS; when larger apertures are used, even if still inside the H II regions, line ratios similar to what was observed by MaNGA and SDSS are derived. This is due to a radial gradient in $[\text{SII}]\lambda 6717,31/\text{H}\alpha$ inside the H II regions.

The strong gradient of the $[\text{SII}]\lambda 6717,31/\text{H}\alpha$ ratio can also be directly seen in the maps of line ratio, exhibiting minima close to the peak of $\text{H}\alpha$ emission and showing that seeing-limited observation of these galaxies can resolve the H II regions.

These results show that the difference between spectra of local H II regions and more distant galaxies is not due to contamination from the DIG but by the smaller angular size of the slit with respect to the projected size of the H II regions. As a consequence, the similar spectra of local and distant galaxies implies that the DIG has a secondary effect on the total spectra of star-forming galaxies. Ongoing and future large IFU surveys of local galaxies with VLT/MUSE (e.g. PHANGS, Schinnerer et al. 2019) and SDSS-V (Kollmeier et al. 2019) are providing a large number of resolved spectra of H II regions with high S/N ratio, large spectral coverage, and across a large range of physical properties to better understand the radial and integrated emission of the H II regions and their separation with the DIG.

ACKNOWLEDGEMENTS

We thank E. Wisnioski and K. Kreckel for sharing their data on H II sizes with us, and the anonymous referee for helping improving the manuscript. FM, GC, and AM acknowledge support from the INAF PRIN-SKA 2017 programme 1.05.01.88.04, and from PRIN MIUR project ‘Black Hole winds and the Baryon Life Cycle of Galaxies: the stone-guest at the galaxy evolution supper’, contract 2017PH3WAT. RM and MC acknowledge support by the Science and Technology Facilities Council (STFC) and ERC Advanced Grant 695671 ‘QUENCH’.

DATA AVAILABILITY

The raw and reduced MUSE data underlying this article are available in the ESO archive services.

REFERENCES

- Abazajian K. N. et al., 2009, *ApJS*, 182, 543
- Aguado D. S. et al., 2019, *ApJS*, 240, 23
- Anand G. S. et al., 2021, *AJ*, 162, 80
- Annibali F., Tosi M., Pasquali A., Aloisi A., Mignoli M., Romano D., 2015, *AJ*, 150, 143
- Arsenault R., Roy J. R., 1988, *A&A*, 201, 199
- Beaton R. L. et al., 2014, *ApJ*, 790, 117
- Belfiore F. et al., 2016, *MNRAS*, 461, 3111
- Belfiore F. et al., 2019, *AJ*, 158, 160
- Berg D. A., Skillman E. D., Croxall K. V., Pogge R. W., Moustakas J., Johnson-Groh M., 2015, *ApJ*, 806, 16
- Berg D. A., Pogge R. W., Skillman E. D., Croxall K. V., Moustakas J., Rogers N. S. J., Sun J., 2020, *ApJ*, 893, 96
- Bradley T. R., Knapen J. H., Beckman J. E., Folkes S. L., 2006, *A&A*, 459, L13
- Bundy K. et al., 2015, *ApJ*, 798, 7
- Byler N., Dalcanton J. J., Conroy C., Johnson B. D., Choi J., Dotter A., Rosenfield P., 2019, *AJ*, 158, 2
- Choi J., Dotter A., Conroy C., Cantiello M., Paxton B., Johnson B. D., 2016, *ApJ*, 823, 102
- Collins J. A., Rand R. J., 2001, *ApJ*, 551, 57
- Conroy C., Gunn J. E., White M., 2009, *ApJ*, 699, 486
- Cosens M. et al., 2018, *ApJ*, 869, 11
- Croxall K. V., Pogge R. W., Berg D. A., Skillman E. D., Moustakas J., 2015, *ApJ*, 808, 42
- Croxall K. V., Pogge R. W., Berg D. A., Skillman E. D., Moustakas J., 2016, *ApJ*, 830, 4
- Curti M., Mannucci F., Cresci G., Maiolino R., 2020, *MNRAS*, 491, 944
- Della Bruna L. et al., 2020, *A&A*, 635, A134
- Dopita M. A., Rich J., Vogt F. P. A., Kewley L. J., Ho I. T., Basurah H. M., Ali A., Amer M. A., 2014, *Ap&SS*, 350, 741
- Dotter A., 2016, *ApJS*, 222, 8
- Ferguson A. M. N., Wyse R. F. G., Gallagher J. S. I., Hunter D. A., 1996, *AJ*, 111, 2265
- Ferland G. J. et al., 2013, *RMxAA*, 49, 137
- Ferreiro D. L., Pastoriza M. G., 2004, *A&A*, 428, 837
- Giammanco C., Beckman J. E., Zurita A., Relaño M., 2004, *A&A*, 424, 877
- Haffner L. M. et al., 2009, *Rev. Mod. Phys.*, 81, 969
- Helmboldt J. F., Walterbos R. A. M., Bothun G. D., O'Neil K., 2005, *ApJ*, 630, 824
- Hidalgo-Gómez A. M., 2005, in Hidalgo-Gómez A. M., González J. J., Rodríguez Espinosa J. M., Torres-Peimbert S., eds, *Revista Mexicana de Astronomía y Astrofísica Conference Series Vol. 24*, Revista Mexicana de Astronomía y Astrofísica Conference Series. p. 288
- Hoopes C. G., Walterbos R. A. M., 2003, *ApJ*, 586, 902
- Hoopes C. G., Walterbos R. A. M., Greenwalt B. E., 1996, *AJ*, 112, 1429
- Kauffmann G. et al., 2003, *MNRAS*, 346, 1055
- Kennicutt R. C. J., 1984, *ApJ*, 287, 116
- Kewley L. J., Heisler C. A., Dopita M. A., Lumsden S., 2001, *ApJS*, 132, 37
- Kewley L. J., Groves B., Kauffmann G., Heckman T., 2006, *MNRAS*, 372, 961
- Kewley L. J., Nicholls D. C., Sutherland R. S., 2019, *ARA&A*, 57, 511
- Kollmeier J. et al., 2019, *Bulletin of the American Astronomical Society*. p. 274
- Kreckel K. et al., 2019, *ApJ*, 887, 80
- Kumari N., Maiolino R., Belfiore F., Curti M., 2019, *MNRAS*, 485, 367
- Lacerda E. A. D. et al., 2018, *MNRAS*, 474, 3727
- Law D. R. et al., 2021, *ApJ*, 915, 35
- Levesque E. M., Kewley L. J., Larson K. L., 2010, *AJ*, 139, 712
- Luridiana V., Morisset C., Shaw R. A., 2015, *A&A*, 573, A42
- Maiolino R., Mannucci F., 2019, *A&A Rev.*, 27, 3
- Mannucci F., Cresci G., Maiolino R., Marconi A., Gnerucci A., 2010, *MNRAS*, 408, 2115
- Marasco A. et al., 2020, *A&A*, 644, A15
- Mingozzi M. et al., 2020, *A&A*, 636, A42
- Minter A. H., Balser D. S., 1997, *ApJ*, 484, L133
- Oey M. S., Parker J. S., Mikles V. J., Zhang X., 2003, *AJ*, 126, 2317
- Oey M. S. et al., 2007, *ApJ*, 661, 801
- Peimbert M., Peimbert A., Delgado-Inglada G., 2017, *PASP*, 129, 082001
- Pellegrini E. W., Oey M. S., Winkler P. F., Points S. D., Smith R. C., Jaskot A. E., Zastrow J., 2012, *ApJ*, 755, 40
- Pilyugin L. S., Grebel E. K., Mattsson L., 2012, *MNRAS*, 424, 2316
- Pilyugin L. S., Grebel E. K., Kniazev A. Y., 2014, *AJ*, 147, 131
- Rand R. J., 1998, *ApJ*, 501, 137
- Reynolds R. J., 1984, *ApJ*, 282, 191
- Rogers N. S. J., Skillman E. D., Pogge R. W., Berg D. A., Moustakas J., Croxall K. V., Sun J., 2021, *ApJ*, 915, 21
- Rossa J., Dettmar R. J., 2003, *A&A*, 406, 493
- Rozas M., Richer M. G., López J. A., Relaño M., Beckman J. E., 2006, *A&A*, 455, 539
- Sabbi E. et al., 2018, *ApJS*, 235, 23
- Sánchez S. F. et al., 2012, *A&A*, 538, A8
- Sanders R. L., Shapley A. E., Zhang K., Yan R., 2017, *ApJ*, 850, 136
- Sanders R. L. et al., 2019, *ApJ*, preprint ([arXiv:1910.13594](https://arxiv.org/abs/1910.13594))
- Schinnerer E. et al., 2019, *The Messenger*, 177, 36
- Tomicic N. et al., 2021, preprint ([arXiv:2108.12433](https://arxiv.org/abs/2108.12433))
- Tomičić N. et al., 2021, *ApJ*, 907, 22
- Tremonti C. A. et al., 2004, *ApJ*, 613, 898
- Tüllmann R., Dettmar R. J., 2000, *A&A*, 362, 119
- Vale Asari N., Couto G. S., Cid Fernandes R., Stasińska G., de Amorim A. L., Ruschel-Dutra D., Werle A., Florido T. Z., 2019, *MNRAS*, 489, 4721
- Voges E. S., Walterbos R. A. M., 2006, *ApJ*, 644, L29
- Westfall K. B. et al., 2019, *AJ*, 158, 231
- Wisnioski E., Glazebrook K., Blake C., Poole G. B., Green A. W., Wyder T., Martin C., 2012, *MNRAS*, 422, 3339
- Xiao L., Stanway E. R., Eldridge J. J., 2018, *MNRAS*, 477, 904
- Youngblood A. J., Hunter D. A., 1999, *ApJ*, 519, 55
- Zhang K. et al., 2017, *MNRAS*, 466, 3217
- Zurita A., Rozas M., Beckman J. E., 2000, *A&A*, 363, 9

This paper has been typeset from a $\text{\TeX}/\text{\LaTeX}$ file prepared by the author.